Int. J. Heat Mass Transfer. Vol. 36, No. 5, pp. 1219–1229, 1993
Printed in Great Britain

0017–9310/93 $6.00 + 0.00

Transient reflectivity measurements and heat transfer modeling in laser annealing of semiconductor films

C. P. GRIGOROPOULOS, A. A. ROSTAMI,† X. XU, S. L. TAYLOR and H. K. PARK

Department of Mechanical Engineering, University of California, Berkeley, CA 94720, U.S.A.

(*Received* 21 *January* 1992 *and in final form* 29 *May* 1992)

Abstract—Melting and solidification of a silicon film by continuous wave laser beam irradiation has been studied. The silicon film melting and recrystallization is controlled by the temperature distribution in the semiconductor. Numerical calculations have been carried out for a range of laser beam parameters and material translational speeds. The results for the melt pool size have been compared with experimental data. The temperature field development has also been monitored with localized reflectivity measurements. Experimental and predicted transient reflectivity distributions have been compared.

1. INTRODUCTION

THE SILICON microfabrication technology has grown rapidly during the past several years. Examples of such advancements are silicon-based sensors, actuators, and other micromechanical devices. Recrystallization of semi-conductor films deposited on amorphous substrates has been shown to improve the transport properties and the reliability of electronic devices [1]. The use of light sources to melt and subsequently recrystallize thin semiconductor layers on insulators, such as oxidized wafers and bulk amorphous substrates has shown good potential for applications to commercial VLSI technology [2]. The crystal growth in silicon film melting and solidification is mainly controlled by the temperature distribution in the semiconductor material. The heat transfer depends on the laser beam total power, the lateral distribution of the beam intensity and the translational speed of the target material. Experimental studies [3] have shown some success in controlling crystal growth by modifying the laser beam shape, and thus the induced temperature field.

Analytical solutions for solid–liquid phase change problems can be found in the literature [4]. Such solutions address specific problems and therefore have a limited range of applicability. Various numerical techniques have been developed to solve solid–liquid phase change problems [5]. One-dimensional phase change finite difference models have been applied to laser annealing of thin semiconductor films [6, 7]. Approximate solutions for the temperature distribution of thin silicon layers by scanning laser beams of elliptical or circular symmetry have also been derived [8, 9]. A three-dimensional transient numerical algorithm for thin silicon laser melting and recrystallization [10] has been based on the conventional enthalpy method [11, 12].

In this study, an explicit finite difference scheme incorporating the enthalpy formulation has been employed to calculate the temperature distributions in the structure and the location of the solid–liquid interface in a thin silicon film deposited on a glass substrate. A portion of the net energy transferred to a partially molten mesh element is consumed to phase change, the rest contributes to the sensible energy. The conventional enthalpy method is modified to account for this effect. The numerical predictions are compared to experimental results for the steady-state molten pool size. An experimental procedure for obtaining *in situ* localized transient surface reflectivity measurements is described. Thin film optics calculations show that the temperature dependence of the silicon complex refractive index produces a strong variation of the film reflectivity with temperature. This variation enables comparison of acquired reflectivity signals to predicted reflectivity distributions.

2. EXPERIMENTAL PROCEDURE

Figure 1 shows a sketch of the sample geometry examined in the experiments. The samples were prepared using Low Pressure Chemical Vapor Deposition (LPCVD). An undoped polysilicon layer of thickness $d_{si} = 0.5\ \mu m$ is deposited on a fused quartz substrate. The substrate has a thickness $d_{ss} = 0.5$ mm. The silicon film is encapsulated by a 0.5 μm-thick SiO_2 layer. Both the substrate and the encapsulating layer are transparent to the wavelength of the laser source. The samples were processed using the apparatus shown in Fig. 2. The annealing beam was produced

†Permanent address: Department of Mechanical Engineering, Isfahan University of Technology, Isfahan, Iran.

NOMENCLATURE

A	absorptivity
c_p	specific heat
d	$d_{enc}+d_{si}$
d_{enc}	encapsulating layer thickness
d_{si}	silicon film thickness
d_{ss}	substrate thickness
e	enthalpy per unit volume
f_l	liquid volume fraction
h_b, h_t	heat transfer coefficients at the bottom and top structure surfaces
i	imaginary unit
k	thermal conductivity
L	latent heat of fusion per unit volume
$\mathcal{M}$	characteristic transmission matrix
n	real part of the complex refractive index
$\hat{n}$	complex refractive index
n_w	number of laser beam peak wavelengths
P_T	total power of laser beam
q_{abs}	absorbed heat flux
q_{cd}	conduction heat loss
q_{cv}	convection heat loss
q_{rad}	radiation heat loss
$q_{\lambda i}$	laser light source irradiance distribution
$q^0_{\lambda i}$	peak power intensity of the laser beam
R	reflectivity
R_g	ray-tracing expression for the substrate reflectivity
R_{total}	total reflectivity
R_{s1}, R_{1s}	reflectivities at the quartz–air, and air–quartz interfaces
R_{1fs}, R_{sf1}	reflectivities of the thin film structure on an infinite substrate for laser light illumination: (a) through the thin films; (b) through the substrate
$R_{\lambda i}$	reflectivity for the λi annealing laser beam wavelength
t	time
T	temperature
T_{bp}	boiling point of silicon
T_m	melting point of silicon
T_∞	initial and ambient temperature
V	velocity of target in x-direction
W	distance from the laser beam center to the point where the intensity of the laser beam drops to $1/e$ of the peak value
x	coordinate in the scanning direction (Fig. 1)
X_s	x-coordinate of the solid–liquid interface
y	coordinate in the transverse direction (Fig. 1)
Y_s	y-coordinate of the solid–liquid interface
z	coordinate normal to the sample surface.

Greek letters

ε_f	film emissivity
ε_{ss}	bottom substrate surface emissivity
λ	wavelength
ρ	density
σ	Stefan–Boltzmann constant
τ	transmissivity
τ_g	ray-tracing expression for the substrate transmissivity
τ_{s1}, τ_{1s}	transmissivities through the quartz–air, air–quartz interfaces
τ_{sf1}, τ_{1fs}	transmissivities of the thin film structure on an infinite substrate for laser light illumination: (a) through the substrate; (b) through the thin films.

Subscripts

enc	encapsulating layer
f	region of lumped layers
i	inner region
l	liquid silicon
o	outer region
s	solid silicon
si	silicon
ss	substrate
1	region of air above the encapsulating layer
2	region of air below the substrate
λb, λi	components of a multi-line laser beam at the $\lambda = 488$ nm, and $\lambda = \lambda i$ $(i = 1, \ldots, n_w)$ wavelengths.

Superscripts

+	illumination through the thin film structure
−	illumination through the substrate
′	value at the new time.

by a continuous wave (CW) argon ion laser. The laser was used either in the multi-line mode, or as a single line source at a wavelength, $\lambda = 514.5$ nm (green light). The maximum power emitted from the laser aperture associated with this wavelength is about 2.5 W. The laser operates in the TEM_{00} mode and the output beam has a Gaussian intensity distribution. A beamsplitter is used to provide a reference signal corresponding to the annealing laser power. The laser beam is focused by a spherical lens with a focal length of 7 cm. The $1/e$ irradiance radius of the annealing beam was measured using the rotating chopper technique presented in ref. [10]. A Gaussian laser beam envelope, defined by a minimum beam radius and a focal waist position was fitted by a least-squares error minimization to the experimental data. The radius of

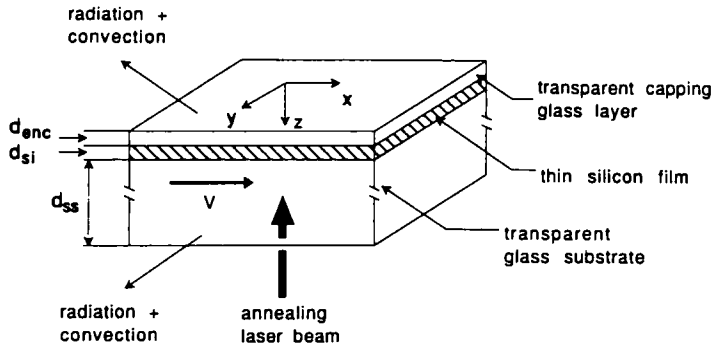

FIG. 1. Sketch of the basic structure studied in this work.

the focal waist on the Gaussian fit is 19.3 μm. The experimentally measured minimum beam radius was 17.4 μm. Point by point comparison of experimental data showed a variation of $\pm 7\%$.

Normal reflectivity measurements are made using the apparatus shown in Fig. 2. Details of the reflectivity microprobe have been described in [13]. A HeNe laser of 5 mW nominal power is used as the probing beam. This source emits at a wavelength, $\lambda = 632.8$ nm (red light). The probing beam is focused on the

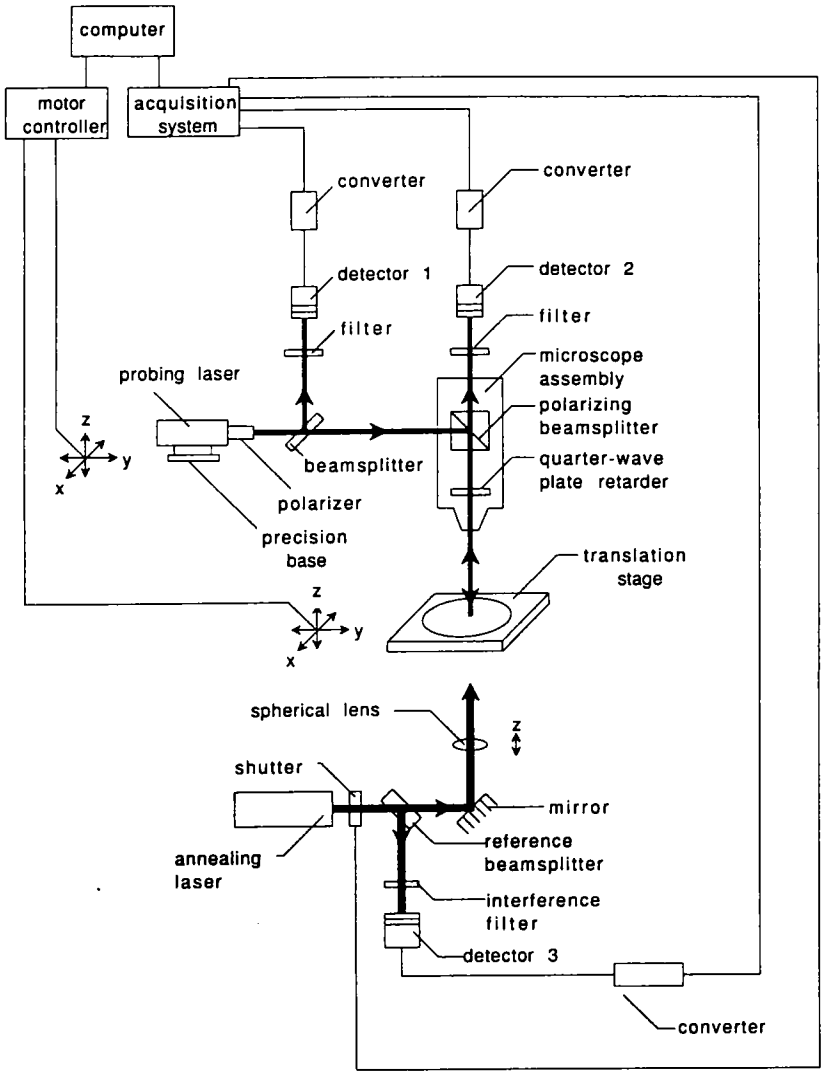

FIG. 2. Schematic of the laser annealing apparatus.

sample by a 30× microscope objective lens with a focal length of 6 mm. Using experimental techniques and Gaussian laser beam theory, the $1/e$ irradiance radius corresponding to the focal waist was determined to be 4.3 μm. As a result, the spatial resolution of the microprobe is about 9 μm. The localized reflectivity measurement experiments were performed with the sample placed at the focal waist of the probing laser beam. The reflectivity microprobe can be moved in a plane parallel to the sample by two piezoelectric motors. The repeatable positioning accuracy of these motors is 1 μm. The accuracy of the reflectivity microprobe apparatus was checked by measuring the reflectivity of oxidized crystalline silicon wafers, which were well characterized by ellipsometry. The reflectivity of these samples was measured by placing a HeNe laser head at a distance of about 2 m from the sample surface. The HeNe laser beam was incident on the sample at a small angle ($\sim 0.3^\circ$) with respect to the normal and the sample surface. These measurements and the reflectivity microprobe measurements were in close agreement (absolute reflectivity deviation within 0.005).

In these experiments, the data acquisition system and the electronic instrumentation and control have been designed to capture the transient effects. Signals from the reflected light, detector 1, and the annealing laser beam reference, detector 3, are measured by a digitizing oscilloscope. The probing laser beam reference, detector 3, is measured using the high speed voltmeter accessory of a data acquisition contol unit. The acquisition frequency for both devices is set to 100 kHz. A computer controller uses internal triggering commands and a two-channel function generator accessory to simultaneously trigger the electronic shutter and the data acquisition hardware. The time for full shutter opening is less than 0.2 ms.

3. THIN FILM OPTICS

Thin film optical theory is used to derive the optical properties of the sample structure. The encapsulation layer and the polysilicon film are sufficiently thin for wave optics to be important. The substrate, however, has a large thickness to wavelength ratio, d_s/λ, so that light interference effects in that region are smoothed out by variations of the substrate thickness and flatness. Electromagnetic wave interference must therefore be considered in the thin films, while light reflection and transmission in the substrate can be modeled using ray-tracing [14]. The following expressions for reflectivity and transmissivity are obtained for a bare substrate, in the case of normal incidence

$$R_g^+ = R_{1s} + \frac{R_{s2}\tau_{1s}\tau_{s1}}{1 - R_{s1}R_{s2}} \tag{1a}$$

$$\tau_g^+ = \frac{\tau_{1s}\tau_{s2}}{1 - R_{s1}R_{s2}} \tag{1b}$$

where

$$R_{ij} = \frac{(n_i - n_j)^2}{(n_i + n_j)^2} \tag{2a}$$

$$\tau_{ij} = 1 - R_{ij} \tag{2b}$$

for $i, j = 1, 2$, or s.

The characteristic transmission matrix, $\mathcal{M}_j$ [15], representing an absorbing thin layer of thickness d_j, and having a complex refractive index, $\hat{n}_j$, is given by

$$\mathcal{M}_j = \begin{bmatrix} \cos\left(\frac{2\pi}{\lambda}\hat{n}_j d_j\right) & -\frac{i}{\hat{n}_j}\sin\left(\frac{2\pi}{\lambda}\hat{n}_j d_j\right) \\ -i\hat{n}_j \sin\left(\frac{2\pi}{\lambda}\hat{n}_j d_j\right) & \cos\left(\frac{2\pi}{\lambda}\hat{n}_j d_j\right) \end{bmatrix}. \tag{3}$$

The two-layer transmission matrix, $\mathcal{M}_f^+$, for light emanating from region 1 is

$$\mathcal{M}_f^+ = \mathcal{M}_{enc} \times \mathcal{M}_{si}. \tag{4}$$

The reflection and transmission coefficients, r, and t_r, are

$$r_f^+ = \frac{(\mathcal{M}_f^+(1,1) + \mathcal{M}_f^+(1,2)n_s) - (\mathcal{M}_f^+(2,1) + \mathcal{M}_f^+(2,2)n_s)}{(\mathcal{M}_f^+(1,1) + \mathcal{M}_f^+(1,2)n_s) + (\mathcal{M}_f^+(2,1) + \mathcal{M}_f^+(2,2)n_s)} \tag{5a}$$

$$t_{r;f}^+ = \frac{2}{(\mathcal{M}_f^+(1,1) + \mathcal{M}_f^+(1,2)n_s) + (\mathcal{M}_f^+(2,1) + \mathcal{M}_f^+(2,2)n_s)}. \tag{5b}$$

The film reflectivity and transmissivity in terms of r_f^+ and $t_{r;f}^+$, follow

$$R_{1fs} = |r_f^+|^2 \tag{6a}$$

$$\tau_{1fs} = n_s |t_{r;f}^+|^2. \tag{6b}$$

Let R_{sf1} and τ_{sf1} be the two-film reflectivity and transmissivity, but for light propagating in the substrate–film–air direction. Equations (1a) and (1b) then yield the following expressions for the structure total reflectivity and transmissivity

$$R_{total}^+ = R_{1fs} + \frac{R_{s2}\tau_{1fs}\tau_{sf1}}{1 - R_{sf1}R_{s2}} \tag{7a}$$

$$\tau_{total}^+ = \frac{\tau_{1fs}\tau_{s2}}{1 - R_{sf1}R_{s2}}. \tag{7b}$$

The above expression for the structure reflectivity is identical to the result derived in ref. [16] by averaging phase effects through the substrate. The annealing laser beam illuminates the sample through the substrate. The substrate reflectivity (R_g^-) can be calculated using ray-tracing

$$R_g^- = R_{2s} + \frac{R_{s1}\tau_{2s}\tau_{s2}}{1 - R_{s2}R_{s1}}. \tag{8}$$

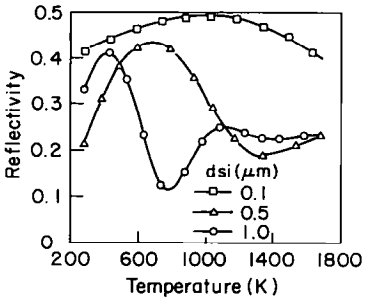

FIG. 3. Predicted normal incidence reflectivity R^{+}_{total} of the sample structure for different silicon film thicknesses, as a function of the silicon layer temperature. The sample is illuminated by the probing laser beam.

The total reflectivity is obtained by replacing R_{s1} with R_{sf1}, which corresponds to light propagation in the polysilicon/SiO_2 structure

$$R^{-}_{\text{total}} = R_{2s} + \frac{R_{sf1}\tau_{2s}\tau_{s2}}{1 - R_{s2}R_{sf1}}. \tag{9}$$

Figure 3 shows the predicted reflectivities for the probing laser beam for different silicon film thicknesses. The data given in ref. [17] for the bulk-form crystalline silicon film complex refractive index have been used in the calculations. The liquid silicon refractive index [18] is used to determine the reflectivity of molten silicon. A reflectivity value of 0.57 is expected for the annealing laser beam ($\lambda = 514.5$ nm) when the thin silicon film has melted.

4. COMPUTATIONAL ANALYSIS

The absorbed laser energy generates a temperature distribution in the silicon film. Heat is lost by convection and radiation from the top and bottom surfaces of the structure. An x–y–z system of Cartesian coordinates is considered fixed on the annealing laser beam center, with the origin at the top encapsulating layer surface, and the z-coordinate pointing into the substrate (Fig. 1). The target may travel with a speed, V, in the x-direction. An infinite computational domain is assumed in the x- and y-directions. The silicon film and the capping layer are sufficiently thin, so that temperature variations in the z-direction across these layers may be neglected for the millisecond time scales considered in this work. The two layers can therefore be considered as lumped, so that the numerical stability requirement is relaxed, and the computing time reduced, without any significant loss of accuracy. The heat conduction equation in region f, the lumped layer region, may be written as

$$(\rho c_p)_f\left(\frac{\partial T_f}{\partial t} + V\frac{\partial T_f}{\partial x}\right) = \frac{\partial}{\partial x}\left(k_f\frac{\partial T_f}{\partial x}\right) + \frac{\partial}{\partial y}\left(k_f\frac{\partial T_f}{\partial y}\right) + \frac{q_{\text{abs}} - (q_{\text{rad}} + q_{\text{cv}} + q_{\text{cd}})}{d} \tag{10}$$

where $d = d_{si} + d_{enc}$. The target is assumed to travel in the x-direction. The heat conduction equation in the substrate is

$$(\rho c_p)_{ss}\left(\frac{\partial T_{ss}}{\partial t} + V\frac{\partial T_{ss}}{\partial x}\right) = \frac{\partial}{\partial x}\left(k_{ss}\frac{\partial T_{ss}}{\partial x}\right) + \frac{\partial}{\partial y}\left(k_{ss}\frac{\partial T_{ss}}{\partial y}\right) + \frac{\partial}{\partial z}\left(k_{ss}\frac{\partial T_{ss}}{\partial z}\right). \tag{11}$$

The boundary conditions are

$$x \to \pm\infty, \qquad T_f = T_{ss} = T_\infty$$
$$y \to \pm\infty, \qquad T_f = T_{ss} = T_\infty$$
$$z = d, \qquad T_f = T_{ss}$$
$$z = d + d_{ss}, \qquad -k_{ss}\frac{\partial T}{\partial z} = h_b(T_{ss} - T_\infty) + \bar{\varepsilon}_{ss}\sigma(T^4_{ss} - T^4_\infty).$$

Initially, the temperature is T_∞ everywhere. The lumped layer volumetric specific heat, $(\rho c_p)_f$, is given by

$$(\rho c_p)_f = \frac{(\rho c_p)_{enc}d_{enc} + (\rho c_p)_{si}d_{si}}{d}. \tag{12}$$

The equivalent lumped layer thermal conductivity, k_f, is calculated considering a local network of thermal resistances. Changes in the thermal conductivity between the solid and liquid silicon are thus taken into account. The laser beam energy that is absorbed by the silicon layer is given by

$$q_{\text{abs}}(x, y, T_f) = \sum_{i=1}^{n_w}[1 - R_{\lambda i}(T_f) - \tau_{\lambda i}(T_f)]q_{\lambda i}(x, y) \tag{13}$$

where n_w is the number of laser beam peak wavelengths and $q_{\lambda i}(x, y)$ is the laser light source irradiance distribution. The beam irradiance distribution can be shaped to be elliptical

$$q_{\lambda i}(x, y) = q^0_{\lambda i}\exp\left\{-\left[\left(\frac{x}{W_{\lambda ix}}\right)^2 + \left(\frac{y}{W_{\lambda iy}}\right)^2\right]\right\} \tag{14}$$

or circular as given by

$$q_{\lambda i}(x, y) = q^0_{\lambda i}\exp\left[-\frac{x^2 + y^2}{W^2_{\lambda i}}\right]. \tag{15}$$

The radiation loss from the region f is calculated from

$$q_{\text{rad}} = \sigma\varepsilon_f(T^4_f - T^4_\infty). \tag{16}$$

The hemispherical total emissivity, ε_f, is calculated by analyzing the electromagnetic wave propagation through the multilayer structure, which is considered isothermal and at thermal equilibrium with its surroundings, subjected to blackbody irradiation. Light absorption and emission are calculated by applying the Poynting vector theorem and Kirchhoff's radi-

ation law. The convection heat loss in equation (10) is given by

$$q_{cv} = h_t(T_f - T_\infty). \tag{17}$$

The heat transfer coefficients, h_t and h_b, are estimated using expressions for free convection from horizontal surfaces. The radiation and the convective losses are very small compared to the laser light absorption in the semiconductor layer. The length scales considered in this problem are small; consequently the thermal gradients are steep, so that conduction is the dominant mode of heat transfer in the solid phase. This is also true for the liquid silicon phase, which is opaque to radiation, exhibiting a metallic behavior. The complete radiative transfer equation does not need to be solved in the multilayer structure as is the case in the large scale vertical Bridgman system for bulk silicon crystal growth [19]. Finally, q_{cd} in equation (10) accounts for the conduction loss to the substrate, which can be calculated using the temperature difference between the grid points on the two sides of the silicon–substrate interface and the equivalent thermal resistance between them. In order to use the enthalpy formulation for the region f, the enthalpy–temperature relation for that region must be established. The enthalpy of the lumped material per unit volume can be written in terms of the enthalpies of its constituents

$$e_f = \frac{e_{enc}d_{enc} + e_{si}d_{si}}{d}. \tag{18}$$

No phase change is considered for the capping SiO_2 layer, and its volumetric heat capacity can be assumed constant

$$e_{enc} = \int_{T_m}^{T} (\rho c_p)_{enc}\, dT = (\rho c_p)_{enc}(T - T_m). \tag{19}$$

For an element of the silicon film completely in solid or liquid phase

$$e_s = \int_{T_m}^{T} (\rho c_p)_{si}\, dT \qquad \text{solid} \tag{20a}$$

$$e_l = \int_{T_m}^{T} (\rho c_p)_{si}\, dT + L \quad \text{liquid.} \tag{20b}$$

If the element of the silicon film contains both phases, an average enthalpy may be defined as

$$e_{si} = f_l e_l + (1 - f_l)e_s \tag{20c}$$

where f_l is the volumetric fraction of the element in the liquid phase. By substituting for e_{enc} and e_{si} in equation (18) from equation (19) and equations (20a)–(20c), a relation between the enthalpy and temperature of a grid point in the lumped region is derived. The enthalpy formulation is used in the phase change zone of the lumped layers. The left-hand side of equation (10) is written in terms of enthalpy

$$\frac{\partial e_f}{\partial t} + V\frac{\partial e_f}{\partial x} = \frac{\partial}{\partial x}\left(k_f \frac{\partial T_f}{\partial x}\right) + \frac{\partial}{\partial y}\left(k_f \frac{\partial T_f}{\partial y}\right) + \frac{q_{abs} - (q_{rad} + q_{cv} + q_{cd})}{d}. \tag{21}$$

The solid–liquid interface location is a function of x, y, and t. At any point on the interface the following conditions apply [20]

$$T_s = T_l = T_m \tag{22}$$

$$\left[1 + \left(\frac{\partial Y_s}{\partial x}\right)^2\right]\left[k_s \frac{\partial T_s}{\partial y} - k_l \frac{\partial T_l}{\partial y}\right] = L\frac{\partial Y_s}{\partial t} \tag{23}$$

$$\left[1 + \left(\frac{\partial X_s}{\partial y}\right)^2\right]\left[k_s \frac{\partial T_s}{\partial x} - k_l \frac{\partial T_l}{\partial x}\right] = L\left(\frac{\partial X_s}{\partial t} - V\right). \tag{24}$$

The computational domain in the x–y plane is divided into the inner region, which contains the liquid material, and the outer region (Fig. 4(a)). Each region is discretized by using a fixed in time orthogonal mesh. For the circular beam intensity profile, the inner region consisted of 21×21 grids located 7 μm apart ($\Delta x_i = \Delta y_i = 7$ μm), while for the elliptic beam profile 45×15 grids of the same size were used. In the outer region grid sizes of either $\Delta x_0 = \Delta y_0 = 50$ μm or $\Delta x_0 = 35$ μm and $\Delta y_0 = 50$ μm were used. The time step used in the calculations was $\Delta t = 4 \times 10^{-7}$ s. The results were virtually identical when a time step, $\Delta t = 2 \times 10^{-7}$ s, was used for the circular beam intensity case and zero translational speed.

Equations (10), (11), and (21) were written in explicit finite difference forms. The enthalpy formulation, equation (21) was only used for the inner region of the lumped layers, where the phase change occurs. For the outer region of the lumped layers the conduction equation (10) was used. The three-dimensional conduction equation (11) was used to solve for the temperature distribution in the substrate. Figure 4(b) shows the solid–liquid interface crossing the volume element (i, j) in the lumped layer region. At time t, the interface S divides the silicon part into a liquid portion $f_l(\Delta x_i \Delta y_i)$ and a solid portion $(1 - f_l)(\Delta x_i \Delta y_i)$. After a small increment in time, Δt, the interface moves to new location S′ resulting in a change of the liquid portion. The progress of the interface can be calculated from the finite difference forms of equations (23) and (24). Once $Y_s'(i)$ and $X_s'(j)$ are calculated, they can be used to obtain the new liquid portion f' at the time $t + \Delta t$. If the interface is in the element at the center of the laser beam, the following equation must be used

$$L\frac{Y_s'(i) - Y_s(i)}{\Delta t} = k_s \frac{T_f(i, j+1) - T_m}{y(j+1) - Y_s(i)} - k_l \frac{T_m - T_f(i, j)}{Y_s(i)}. \tag{25}$$

This equation assumes radial symmetry for the interface as long as its diameter is less than Δx_i. At the

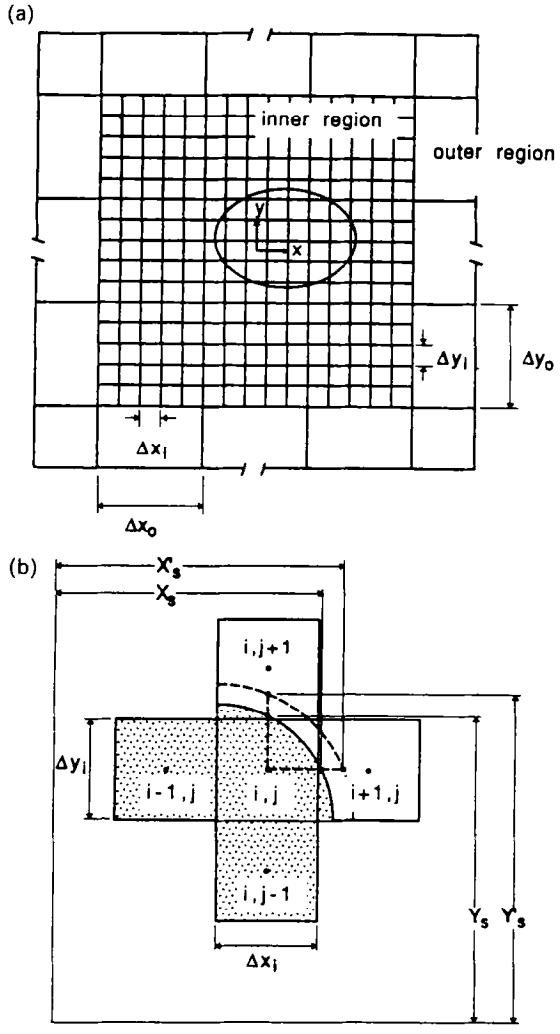

FIG. 4. Top view of the melt pool in the silicon film showing: (a) subdivisions in the physical domain; (b) progress of solid–liquid interface during time Δt.

beginning of melting, when $Y_s(i) = 0$, the last term of equation (25) becomes infinite. This singularity can be removed by writing equation (25) in a backward time difference form. Therefore, for the starting conditions at the beginning of melting

$$L\frac{Y'_s(i)}{\Delta t} = k_s\frac{T'_f(i,j+1)-T_m}{y(j+1)-Y'_s(i)} - k_l\frac{T_m-T'_f(i,j)}{Y'_s(i)}. \tag{26}$$

However, equation (19) has two unknowns, namely $Y'_s(i)$ and $T'_f(i,j)$. The latter can be replaced by the enthalpy $e'_f(i,j)$, using equations (18)–(20). Therefore, equation (26) can be written as

$$L\frac{Y'_s(i)}{\Delta t} = k_s\frac{T'_f(i,j+1)-T_m}{y(j+1)-Y'_s(i)} + \frac{k_l}{(\rho c_p)_f}\frac{e'_f(i,j)-\pi\left(\frac{Y'_s(i)}{\Delta y_i}\right)^2 L\frac{d_{si}}{d}}{Y'_s(i)}. \tag{27}$$

Equation (27) is solved numerically for Y'_s.

The thermal conductivity of the solid silicon varies with temperature [21]

$$k_{si} = 2.99\times10^4/(T-99)\text{W m}^{-1}\text{ K}^{-1} \tag{28}$$

where T is in K. The solid silicon volumetric specific heat is given by [21]

$$(\rho c_p)_{si} = 1.45\times10^6+86\,500(T-270)^{0.23}\text{ J m}^{-3}\text{ K}^{-1}. \tag{29}$$

The thermal conductivity and the volumetric specific heat of the liquid silicon are $k_{si} = 67$ W m^{-1} K^{-1} and $(\rho c_p)_{si} = 2.43\times10^6$ J m^{-3} K^{-1}.

The glass thermophysical properties are $(\rho c_p)_{enc} = (\rho c_p)_{ss} = 2.64\times10^6$ J m^{-1} K^{-1} and $k_{enc} = k_{ss} = 1.4$ W m^{-1} K^{-1}. These values are assumed constant.

Determination of the temperature distributions and the location of the solid–liquid interface involves the following steps: (i) the enthalpy of grid points in the inner region of the lumped layers and the temperature of the grid points in the outer region and the substrate are calculated using the explicit finite difference forms of equations (21), (10) or (11); (ii) prior to any phase change, the temperature of the points in the inner region is calculated from the enthalpies using equations (18), (19) and (20a); (iii) the temperatures of all grid points in the inner region are compared with the melting temperature of silicon. If any of these temperatures is greater than T_m, the solid–liquid interface is assumed to be in that mesh element; (iv) the initial size of the interface is calculated from equation (26). For the subsequent time steps, equation (27) is used to determine the radius of the interface as long as it is less than $\Delta x_i/2$; (v) once the interface passes the boundary of the first mesh, equations (23) and (24) are used to track its progress in the y- and x-directions, respectively; (vi) the new solid–liquid interface is then represented by an interpolating polynomial; (vii) the volume fraction of each subdivision is calculated by integrating the interpolating polynomial; (viii) finally, the temperature of the mesh containing both the solid and liquid phases is calculated from equations (18), (19) and (20c).

5. RESULTS

The calculations were carried out for a range of laser beam parameters. The finite shutter opening time was accounted for in the initial temporal distribution of the incident laser beam energy. The laser beam power was varied from $P_T = 1.0$ to 1.8 W and the beam radius corresponding to $1/e$ intensity, W_{ib}, was varied from 30 to 80 μm. The results have shown that after an elapsed time of 20 ms, a quasi-steady temperature distribution and melt pool size are vir-

tually established. Figure 5(a) shows the temperature rise in a non-moving silicon film, at the center of the laser beam for beam radii of 30, 40, 50, 60, 70, and 80 μm and a total power of 1.8 W. The rate of the temperature increase is reduced after the beginning of melting. This effect is pronounced for the larger beam radii for which the radial variation of the beam intensity is milder. The change in the temperature rise after the initiation of phase change is also due to a larger thermal conductivity of liquid silicon than that of the solid silicon at the melting temperature. It is also caused by a drop in the absorption of the silicon film by almost 40% as a result of phase change to liquid. For $W_{\lambda b} = 30$ μm, the silicon temperature at the center reaches the boiling point, $T_{bp} = 2628$ K, within 5 ms. This is related to the 'keyhole' formation observed in the experiments [10]. The numerical scheme does not consider this effect. The computations indicate that the substrate temperature in the vicinity of the silicon layer, as well as the encapsulating layer temperature, may rise above the softening point, which for fused silica is about 1850 K [22]. Specific transition temperatures with accompanying latent heats of fusion are not available for glass materials, and thus are not taken into account. Figure 5(b) shows the melt pool size for the same parameters as in Fig. 5(a). As the beam radius is increased, the beginning of melting is delayed. Figure 6(a) gives the radial distribution of the silicon temperature at $t = 20$ ms. At $W_{\lambda b} = 80$ μm, the temperature across the molten zone is almost uniform, and stays close to the melting point. The temperature penetration into the substrate is depicted in Fig. 6(b).

Figure 7(a) shows the melt pool for $W_{\lambda b} = 53$ μm and a sample translational speed, $V = 2$ mm s^{-1}. At $V = 2$ mm s^{-1} the shape of the pool is only slightly distorted due to the effect of the translational speed of the target material. The calculated diameter in the x-direction is 112.4 μm and the diameter in the y-direction is 110.6 μm. The experimental value of the average molten pool diameter was 119 μm, indicating a relatively good agreement between the numerical and experimental results. Figure 7(b) shows the melt pool size for the same laser beam parameters and $V = 40$ mm s^{-1}, respectively. As the translational speed is increased, the melt pool becomes smaller, and the elapsed time for achieving quasi-steady conditions is shorter. At the larger beam diameters (at $P_T = 1.8$ W, this occurs in the neighborhood of $W_{\lambda b} = 70$–80 μm) partial melting was observed. The partially molten zone contains liquid coexisting with solid filaments [23]. The present numerical scheme does not address this phenomenon, since it assumes that the molten zone contains only the uniformly liquid phase. As the temperature gradients across the solid–liquid

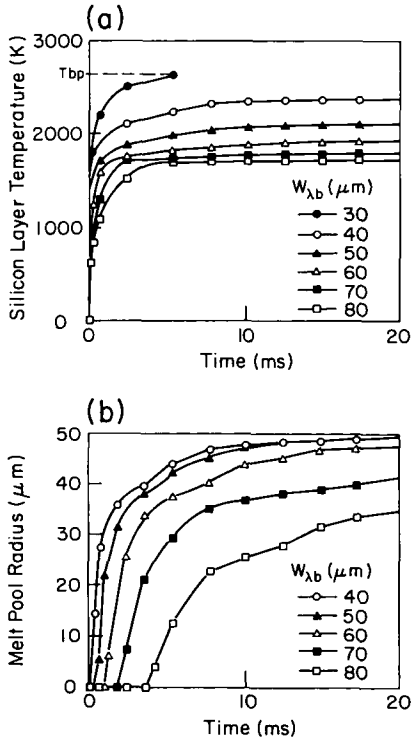

FIG. 5. (a) Silicon temperature at the center of the laser beam, and (b) melt pool radius for $P_T = 1.8$ W, $W_{\lambda b} = 30$, 40, 50, 60, 70 and 80 μm and $V = 0$ mm s^{-1}.

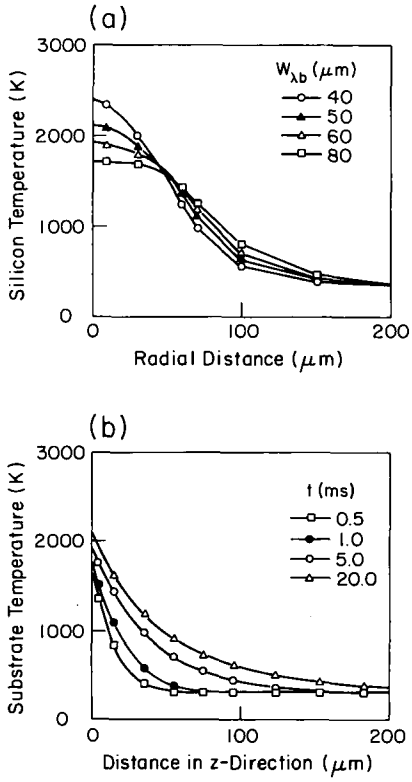

FIG. 6. (a) Radial distribution of the silicon temperature for $P_T = 1.8$ W, $W_{\lambda b} = 40$, 50, 60 and 80 μm at $t = 20$ ms, and $V = 0$ mm s^{-1}. (b) Temperature profiles in the substrate along the centerline of the laser beam at $t = 0.5$, 1, 5, 20 ms, for $P_T = 1.8$ W, $W_{\lambda b} = 50$ μm, and $V = 0$ mm s^{-1}.

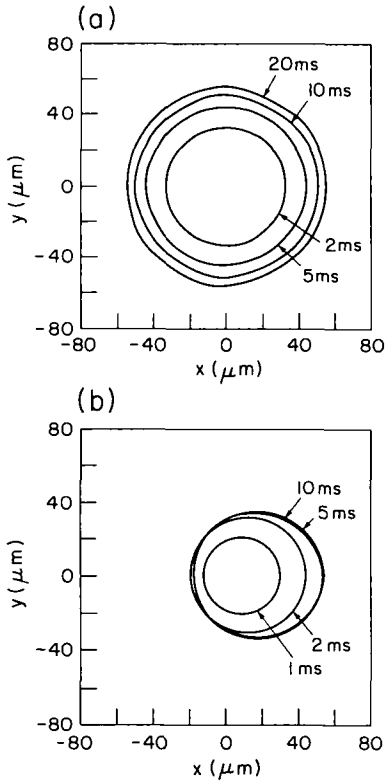

FIG. 7. Melt pool in the silicon film for $P_T = 1.8$ W, $W_{zb} = 53$ μm: (a) at $t = 2, 5, 10, 20$ ms, $V = 2$ mm s^{-1}; (b) at $t = 1, 2, 5, 10, 20$ ms, $V = 40$ mm s^{-1}.

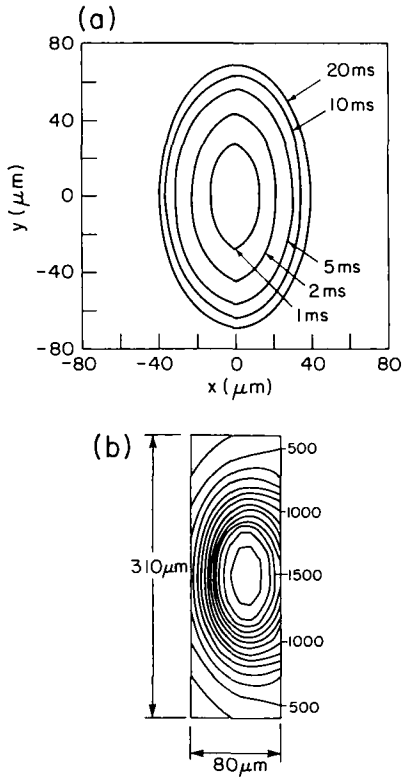

FIG. 8. Melt pool in the silicon film for $P_T = 1.8$ W, $W_{zbx} = 36$ μm, $W_{zby} = 76$ μm: (a) at $t = 1, 2, 5, 10, 20$ ms, $V = 2$ mm s^{-1}; (b) contour plot of the temperature field in the silicon layer at $t = 10$ ms, $V = 40$ mm s^{-1}.

interface decrease, the phase change boundary may become unstable with respect to temperature field perturbations. These instabilities are surface tension limited and may give rise to solid–liquid coexistence [24, 25]. The difference between the experimental data and the numerical results may also be due to departures of the thin film thermal and optical properties from the bulk form values [26, 27].

Figure 8(a) shows the melt pool size for a laser beam with elliptic intensity distribution, with $W_{zbx} = 36$ μm and $W_{zby} = 76$ μm and a speed, $V = 2$ mm s^{-1}. The calculated lengths of the major and minor axes of the elliptically shaped molten pool along the x- and y-directions, at $t = 20$ ms, are 144 and 80 μm, respectively. The corresponding experimental values are 166 and 78 μm. At a material translational speed, $V = 40$ mm s^{-1}, an elliptical laser beam with the same parameters generates the temperature field shown in Fig. 8(b). Steeper temperature field gradients develop ahead of the molten pool due to the sample translation.

The computational predictions of the temperature field can be converted to surface reflectivity response to a HeNe probing laser beam (Section 3). Using the *in situ* normal incidence reflectivity measurement apparatus, transient reflectivity signals are obtained at the laser beam center (Fig. 9(a), and at a point at a distance of 40 μm from the center of the laser beam (Fig. 9(b)). The theoretical predictions yield higher reflectivity values, but indicate the same trends of transient response. The experimental method was applied to the investigation of the phase change process by placing the reflectivity probe at the center of the annealing laser beam. In the case of a laser beam power, $P_T = 1.4$ W, Fig. 10 shows good agreement for the time taken to reach the solid phase reflectivity peak (which is predicted at a temperature of approximately 700 K). On the experimental signal, the transition to melting is not marked by a sharp increase to the liquid silicon value. A positive slope of the reflectivity signal with time is expected, due to the finite size of the probing laser beam. The observed oscillatory trend, however, is interesting. The magnitude and temporal width of the successive reflectivity peaks increase progressively with time. The computations predict melting at a time, $t = 2.3$ ms. On the experimental curve this time corresponds to the beginning of a reflectivity rise. The experiment and the computational prediction at higher laser beam power, $P_T = 1.8$ W, are compared in Fig. 11(a). The oscillatory behavior of the experimental reflectivity trace is a consistent characteristic of the melting process. It indicates that melting of silicon films using optical sources in the visible range is initially nonuniform. As the material begins to melt, there is a tendency to return to the solid phase, because of the

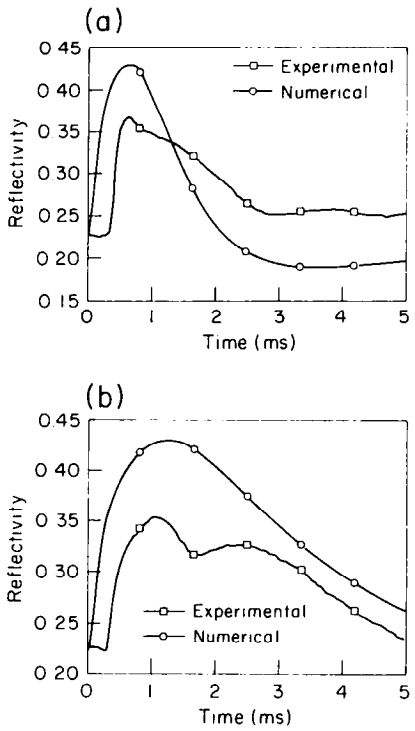

FIG. 9. Transient reflectivity signal histories for a non-moving, 0.5 μm-thick silicon film, heated by a monochromatic argon laser beam, $\lambda = 514.5$ nm, $P_T = 1.0$ W and $W = 60$ μm, obtained by the numerical analysis and the experiment: (a) at the center of the laser beam; (b) at a distance of 40 μm from the center of the beam.

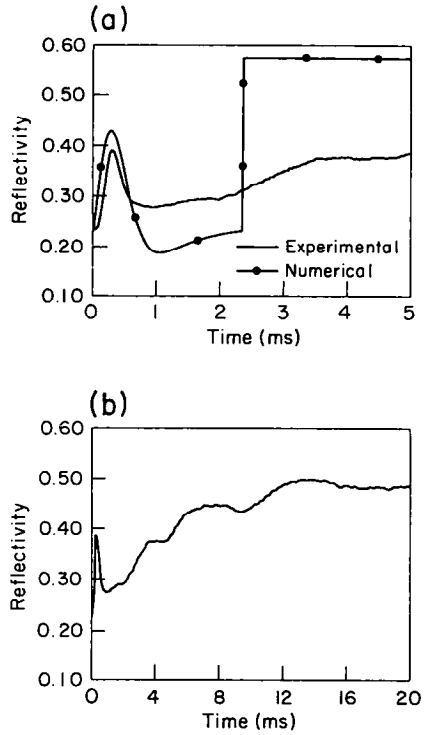

FIG. 10. Comparison of experimental and computational results for a non-moving, 0.5 μm-thick silicon film, heated by a monochromatic argon laser beam with $\lambda = 514.5$ nm, $P_T = 1.40$ W, $W = 60$ μm: (a) over a 5 ms period; (b) over a 20 ms period.

significant laser beam energy absorption decrease with melting. The oscillations are interpreted as representative of a changing liquid–solid fraction in the region sensed by the optical microprobe. After sufficient exposure to the heat source, complete melting is observed (Fig. 11(b)).

6. CONCLUSIONS

The solid–liquid phase change of a silicon film on an amorphous substrate due to the absorption of a CW argon laser beam was studied experimentally and computationally. A technique for acquiring transient, localized, *in situ* reflectivity measurements was developed. The spatial resolution achieved is limited by the spot size of the probing HeNe laser beam, and is about 9 μm. An optics model considering ray-tracing in the substrate and wave interference through the thin film structure was employed to calculate the response to the probing beam, as well as light absorption in the semiconductor layer. The enthalpy formulation for the solution of phase change problems was modified and used to solve for the transient temperature distributions in the film and in the substrate as well as the melt pool size. The results have shown that the temperature distributions and the melt pool size are controlled by the total power and shape of the laser beam, along with the translational speed of the target material. For a given power, the temperature rise after the beginning of melting becomes smaller as the beam radius is increased. The melt pool radius increases with the beam size and decreases after reaching a maximum. For a given beam radius, the temperature of the silicon film and the melt pool size increase with increasing total power. The agreement between the numerical results and the experimental data is good for laser beam intensities that generate uniformly molten pools. The solid–liquid interface is only slightly distorted due to a material translational speed of 2 mm s^{-1}. However, the shape of the melt pool is strongly dependent on the lateral distribution of the laser beam intensity. Computations for higher material translational speeds show phase boundary distortion, molten pool size reduction, and shorter elapsed times for reaching steady-state pool size. The numerical predictions were also compared to localized surface reflectivity measurements with good agreement. The acquired reflectivity signals at the beginning of the phase change process exhibit an oscillatory behavior, which suggests the possibility of initially nonuniform melting. Further improvements depend upon accurate knowledge of thin film optical properties at high temperatures. High speed photography experiments are needed to capture the initial dynamics of the melting process.

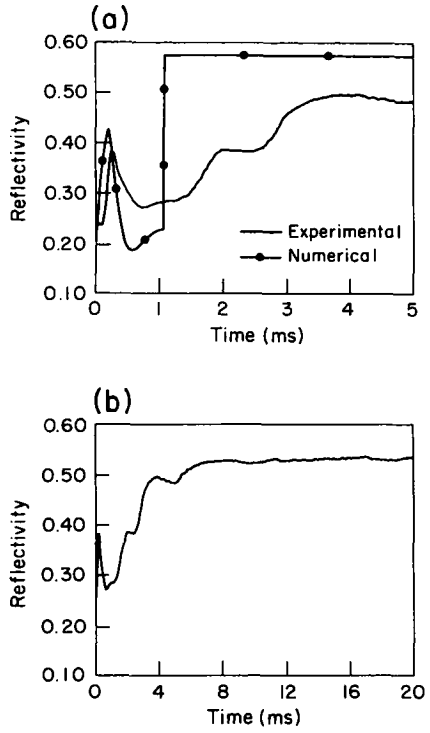

FIG. 11. Comparison of experimental and computational results for a non-moving, 0.5 μm-thick silicon film, heated by a monochromatic argon laser beam with $\lambda = 514.5$ nm, $P_T = 1.80$ W, $W = 60$ μm (a) over a 5 ms period; (b) over a 20 ms period.

Acknowledgement—Support for this work by the National Science Foundation, under Grant CTS-9096253, and in part by the Berkeley Engineering Fund, is gratefully acknowledged.

REFERENCES

1. G. K. Celler, Laser recrystallization of thin films on amorphous insulating substrates, *J. Crystal Growth* **63**, 429–444 (1983).
2. B. Y. Tsaur, Assessment of silicon on insulator technologies for VLSI, *Proc. Materials Research Society* (Edited by A. Chiang, M. W. Geis and L. Pfeiffer), Vol. 53, pp. 365–373. MRS, Pittsburgh, Pennsylvania (1986).
3. T. J. Stultz and J. F. Gibbons, The use of beam shaping to achieve large-grain CW laser-recrystallized polysilicon on amorphous substrates, *Appl. Phys. Lett.* **39**, 498–500 (1981).
4. H. S. Carslaw and J. C. Jaeger, *Conduction of Heat in Solids* (2nd Edn), pp. 282–296. Oxford University Press, Oxford (1959).
5. J. R. Ockendon and W. R. Hodgkins, *Moving Boundary Problems in Heat Flow and Diffusion*. Oxford University Press, Oxford (1975).
6. K. Kubota, C. E. Hunt and J. Frey, Thermal profiles during recrystallization of silicon on insulator with scanning incoherent light line sources, *Appl. Phys. Lett.* **46**, 1153–1155 (1985).
7. I. N. Miaoulis and B. B. Mikic, Heat source power requirements for high-quality recrystallization of thin silicon films for electronic devices, *J. Appl. Phys.* **59**, 1658–1666 (1986).
8. D. Waechter, P. Schvan, R. E. Thomas and N. G. Tarr, Modeling of heat flow in multilayer CW laser-annealed structures, *J. Appl. Phys.* **59**, 3371–3374 (1986).
9. G. J. Willems, J. J. Poortmans and H. E. Maes, A semi-empirical model for the laser-induced molten zone in the recrystallization process, *J. Appl. Phys.* **62**(8), 3408–3415 (1987).
10. C. P. Grigoropoulos, W. E. Dutcher and A. F. Emery, Experimental and computational analysis of laser melting of thin silicon films, *J. Heat Transfer* **113**, 21–29 (1991).
11. D. R. Atthey, A finite difference scheme for melting problems, *J. Inst. Math. Applic.* **13**, 353–366 (1974).
12. N. Shamsundar and E. M. Sparrow, Analysis of multidimensional conduction phase change via the enthalpy model, *J. Heat Transfer* **97**, 333–340 (1975).
13. C. P. Grigoropoulos, W. E. Dutcher and K. E. Barclay, Radiative phenomena in CW laser annealing, *J. Heat Transfer* **113**, 657–662 (1991).
14. G. Chen and C. L. Tien, Partial coherence theory of thin film radiative properties, presented at the 1991 ASME Winter Annual Meeting, HTD-Vol. 184, pp. 9–20 (1991).
15. M. Born and E. Wolf, *Principles of Optics*, pp. 55–70 (6th Edn). Pergamon Press, Oxford (1980).
16. R. F. Potter, Basic parameters for measuring optical properties. In *Handbook of Optical Constants of Solids* (Edited by E. D. Palik), pp. 11–34. Academic Press, New York (1985).
17. G. E. Jellison and H. H. Burke, The temperature dependence of the refractive index of silicon at elevated temperatures at several laser wavelengths, *J. Appl. Phys.* **60**, 841–843 (1986).
18. K. M. Shvarev, B. A. Baum and P. V. Gel'd, Optical properties of liquid silicon, *Sov. Phys. Solid State* **16**, 2111–2112 (1975).
19. H. Matsushima and R. Viskanta, Effects of internal radiative transfer on natural convection and heat transfer in a vertical crystal growth configuration, *Int. J. Heat Mass Transfer* **33**, 1957–1968 (1990).
20. M. N. Ozisik, *Heat Conduction*, pp. 397–438. Wiley, New York (1980).
21. Y. S. Touloukian, *Thermophysical Properties of Matter, Thermal Conductivities*. Plenum Press, New York (1970).
22. G. W. McLellan and E. B. Shand, *Glass Engineering Handbook*, p. 2.9. McGraw-Hill, New York (1984).
23. M. A. Bosch and R. A. Lemons, Laser induced melt dynamics of Si and silica, *Phys. Rev. Lett.* **47**, 1151–1155 (1981).
24. K. A. Jackson and D. A. Kurtze, Instability in radiatively melted silicon films, *J. Crystal Growth* **71**, 385–390 (1985).
25. C. P. Grigoropoulos, R. H. Buckholz and G. A. Domoto, A thermal instability in the laser-driven melting and recrystallization of thin silicon films on glass substrates, *J. Heat Transfer* **109**, 841–847 (1987).
26. Y. C. Tai, C. H. Mastrangelo and R. S. Muller, Thermal conductivity of heavily doped low-pressure chemical vapor deposited polycrystalline silicon films, *J. Appl. Phys.* **63**, 1442–1447 (1988).
27. B. G. Bagley, D. E. Aspnes, A. C. Adams and C. J. Mogab, Optical properties of low-pressure chemically vapor deposited silicon over the energy range 3.0–6.0 eV, *Appl. Phys. Lett.* **38**, 56–58 (1981).